RSC Advances

ROYAL SOCIETY OF CHEMISTRY

www.rsc.org/advances

Fabrication of a novel ZnO/MMO/CNT nanohybrid derived from multi-cationic layered double hydroxide for photocatalytic degradation of azo dye under visible light

Fatemeh Khodam, Zolfaghar Rezvani*, Ali Reza Amani-Ghadim

Department of Chemistry, Faculty of Basic Sciences, Azarbaijan Shahid Madani University, Tabriz, Iran

Abstract

With the purpose of the enhancement of photocatalytic performance in the visible region and efficient electron−hole separation, we reported a facile method for synthesis of mixed metal oxide/ZnO/CNT (MMO/ZnO/CNT) nanohybrid derived from ZnO/Co-Ni-Al layered double hydroxide (LDH) precursor. The structural and morphological aspects of the synthesized products were characterized by X-ray diffraction, scanning electron microscopy, UV/vis diffuse reflectance spectra, and FT-IR spectroscopy. The photocatalytic activity of synthesized ZnO/MMO/CNT nanohybrid was investigated by photocatalytic degradation of C.I. Acid Red 14, as a model pollutant, under visible light irradiation. The photocatalytic activity of ZnO/MMO/CNT was also compared with TiO_2- P25, ZnO, and ZnO/Co-Ni-Al-LDH /CNT. The experimental results revealed that in comparison with other used photocatalysts, ZnO/MMO/CNT nanohybrid was an efficient photocatalyst under visible light irradiation. The effect of operational parameters including photocatalyst content, dye concentration, pH, and irradiation time on the photocatalytic removal efficiency of dye was investigated and optimized using response surface methodology approach. The photocatalyst dosage of 0.009 g, initial dye concentration of 20 mg/L, pH of 4.12, and irradiation time of 150 min were obtained as the optimum condition. In the proposed optimum condition, the catalyst reusability tests were carried out for five runs. Negligible decrease in degradation efficiency confirmed high potential of stability and reusability for the ZnO/MMO/CNT photocatalyst.

Keywords: Layered double hydroxide, Mixed metal oxide, Nanohybrid, Photocatalyst, RSM.

* Corresponding author: zrezvani@azaruniv.ac.ir, or z_rezvani@yahoo.com, Phone & Fax: +98 413 432 7541

1. Introduction

Photocatalytic advanced oxidation processes (PAOPs) are the eco-friendly techniques, being used for the treatment of persistent organic pollutants. PAOPs were based on irradiation of light with sufficient energy, usually UVC (λ=320–400 nm), for the production of free hydroxyl radicals in the presence of a semiconductor as a photocatalyst. Heterogeneous photocatalysis is a promising destructive technology for the treatment of polluted water because of a number of advantages.[1-5] First, this process can be used under normal conditions such as room temperature and atmospheric pressure. Second, this process can remove the pollutants by decomposing them into non-toxic materials. Finally, it can destroy most of the organic pollutants completely, without causing secondary pollution problems. On the other hand, the PAOPs face two challenges: large energy band gap and low quantum yields. In case of common photocatalysts such as TiO_2 and ZnO, the energy gap between filled valance band and empty conduction band is larger than 3 eV. The valance band electrons are excited by illumination of the UV light (λ< 390 nm) and recombination possibility of the photogenerated $e\text{-}h^+$ pairs results in decrease in quantum efficiency. Many attempts have been carried out in detailed studies for the characterization of various photocatalysts using a number of molecular spectroscopies in order to design and develop photocatalysts which are able to work under visible irradiation. These attempts improve the photocatalytic activity through coupling semiconductor photocatalysts, modifying the surface of the semiconductor with metals and non-metal-ion doping, and etc.[6-12] Carbon nanotubes (CNTs) are cylindrical tubes of graphene material that show exceptional properties such as ultra-low weight, high mechanical strength, thermal and chemical stability, and above all, excellent electrical conductivity for storing and shuttling electron[13,14]. The assembly of carbon nanotube (CNTs)-based hetero structures or hybrids with

the desired nano scale materials in the past decade had great potential to significantly improve the photoinduced electron transfer and photoconversion efficiency, owing to good electron accepting property of the carbon nanotubes.[13,15-20]

Layered double hydroxides (LDHs) are a class of anionic (anion exchanging) clays or hydrotalcite-like compounds [21], consisting of brucite-like materials, in which a fraction of the divalent cations has been replaced isomorphosly by trivalent cations producing positively charged layers and interlayer charge-compensating anionic species or counter ions between the layers. Some hydrogen bonded water molecules may occupy the remaining free space of the interlayer space. These materials are described according to the standard formula: $[M^{II}_{1-x}M^{III}_{x}(OH)_2]^{x+}$ $[X^{m-}_{x/m}.nH_2O]^{x-}$, abbreviated as $[M^{II}$-M^{III}-X], where M^{II} and M^{III} are divalent and trivalent metal ions, respectively, and X^{m-} the interlayer anions with x being defined as the M^{II} /(M^{II} +M^{III}) ratio. Due to the flexible ion-exchangeability and tunable composition, layered double hydroxides have emerged as one of the most promising materials for their unique and attractive properties and feasibility of applications in various fields such as catalysis, photocatalysis, catalyst support, adsorbents and drug delivery systems.[22] LDHs are converted into mixed metal oxides (MMO) after calcination at the temperature range of 300 to 700 ˚C.[23, 24] It was reported that calcined LDHs could be used as photocatalysts for the photodegradation of organic pollutants, taking the form of highly dispersed metal oxides.[13]

In the present work, in order to combine the unique properties of carbon nanotubes with layered double hydroxides to obtain more excellent photocatalytic performance under visible light irradiation, we proposed a model for the synthesis of ZnO/mixed metal oxide/CNT (ZnO/MMO/CNT) nanohybrid that is derived from ZnO/Co-Ni-Al layered double hydroxide (LDH) precursor. The specific objectives of this work were: (1) synthesis and characterization of

the ZnO/MMO/CNT mixed metal oxide nanohybrid, (2) investigation of photocatalytic activity of the synthesized ZnO/MMO/CNT mixed metal oxide nanohybrid for the removal of C.I Acid Red 14 (AR14), as a model organic pollutant, in aqueous solution, and (3) optimization and modeling of photocatalytic performance by response surface methodology (RSM) approach.

2. Experimental

2.1. Materials and instruments

All steps of synthesis were conducted using bidistilled water. The pH values were adjusted by combining different amounts of 1 N solutions of Na_2CO_3 and 0.1 M solution of HNO_3. $NiCl_2.6H_2O$, $CoCl_2.6H_2O$, $AlCl_3.6H_2O$, and $Zn(CH_3COO)_2.2H_2O$ were purchased from Merck chemical company. Pristine MWCNTs with a diameter of 10–20 nm and length of 1 μm was obtained from nano lab (Brighton, MA). ZnO nanoparticles were obtained from Fluka chemical company. TiO_2 nanoparticles (Degussa P-25) were obtained from Sigma Aldrich chemical company. C.I. Acid Red 14 was obtained from Solar Fine Chemical Company (Taiwan). All of the chemicals were used without further purification. Powder x-ray diffraction (PXRD) patterns of the samples were recorded by a Bruker AXS model D8 advanced diffractometer for Cu K_α radiation (λ=1.54187 Å) at 40 kV and 35 mA with Bragg angle ranging from 3 to 70 °. The FTIR spectra were obtained using a Bruker spectrophotometer in the range of 400–4000 cm^{-1}. The pH values were measured by Hana pH-meter model 211. The thermogravimetric analysis (TGA) was carried out by a Mettler Toledo TGA 851e device. The heating rate was 10 °C/min within nitrogen atmosphere. The scanning electron microscopy (SEM) was utilized to study the morphology of some selected samples using ultrahigh resolution FESEM device, model

ULTRA55, Carl Zeiss MST AG. The absorption values of solutions containing AR14 were measured by a Jasco UV-Vis spectrometer model 7850. The point of zero charge pH (pH_{PZC}) of the lepidocrocite was identified according to the salt addition method described by Mustafa et al. [25] Al ,Ni, Zn, and Co contents of the samples were determined by using inductively coupled plasma spectroscopy (Jobin Yvon JY24) after dissolving the samples in nitric acid.

2.2. Synthesis of Co-Ni-Al-Zn/CNT mixed metal oxide (ZnO/MMO/CNT) nanohybrid and Co-Ni-Al-LDH

Negatively charged CNT (CNT-COONa) was prepared according to the literature procedure.[26] Synthesis of the Co-Ni-Al-Zn/CNT mixed metal oxide (ZnO/MMO/CNT) nanohybrid was carried out using the well-known co-precipitation method. 20 mg of CNT-COONa was dispersed in 30 mL of deionized water and was ultrasonicated for 20 min. Then, $NiCl_2.6H_2O$ (0.002 mol), $CoCl_2.6H_2O$ (0.002 mol), and $AlCl_3.6H_2O$ (0.002 mol) (the metal ion molar ratio is 1:1:1) were dissolved in the above-mentioned CNT-COONa dispersion to obtain the mixed solution (solution A). $Zn(CH_3COO)_2.2H_2O$ (0.003 mol) was dissolved in 20 mL deionized water (solution B). Solution B was added dropwise to the stirring solution A. The pH of the solution was adjusted to about 10 by adding 1 N Na_2CO_3. The solution was aged for 72 hrs in an oil bath at 60 ^oC. The resulting precipitate was centrifuged, thoroughly washed by distilled water, and dried in an oven at 40 ^oC overnight. The dried precipitate was calcined at 300 $^{\circ}C$ for 5 h to transform into Co-Ni-Al-Zn/CNT mixed metal oxide (ZnO/MMO/CNT) nanohybrid.

The synthesis of Co-Ni-Al-LDH was similar to that described above, but without using CNT (CNT-COONa) and $Zn(CH_3COO)_2.2H_2O$. After aging of solution for 72 hrs in an oil bath at 60

°C, the resulting precipitate was centrifuged, thoroughly washed by distilled water, and dried in an oven at 40 °C.

2.3. Experimental design and statistical analysis

RSM is a collection of mathematical and statistical techniques utilized for investigating the effects of different variables and their interactions on removal efficiency and optimizing the process.[27] Central composite design (CCD), the most widely used design type, was employed to evaluate the combined effects of four main controllable variables (factors) on the dye removal efficiency (output response).[27] The experimental ranges of the variables are presented in Table 1. The design matrix for experiments performing (Table 2) consists of 16 factorial design points, 8 axial points, and 8 center points to obtain an estimation of the experimental error variance. Minintab 16 software was utilized for experimental data analyzing. The second-order polynomial model (Eq.1) was obtained by fitting the removal efficiencies of all runs (Table 3):

$$y = b_0 + \sum_{i=1}^{n}(b_i x_i) + \sum_{i=1}^{n}(b_{ii} x_{ii}^2) + \sum_{i=1}^{n}(b_{ij} x_i x_j) \quad (1)$$

where y is the predicted degradation efficiency, x_i values are the coded levels of the variable, b_o is a constant, and b_i , b_{ii} and b_{ij} values are the linear, quadratic, and interaction coefficients respectively.

Table1. Independent variables and coded levels used for experimental design.

Variables (Factors)	Symbol	Ranges and actual values of coded levels				
		-α	-1	0	+1	+α
ZnO/MMO/CNT (g)	x_1	0.005	0.008	0.011	0.014	0.017
Time (min)	x_2	30	60	90	120	150
pH	x_3	4	5.5	7	8.50	10
Initial dye concentration (mg/L)	x_4	20	30	40	50	60

Table 2. Central composite design matrix for four variables and degradation efficiency

Run	Coded variables				DE, %	
	ZnO/MMO/CNT (g)	Time (min)	pH	$[Dye]_0$ (mg/L)	Experimental	Predicted
1	0	2	0	0	94.87	94.1404
2	-1	-1	-1	1	68.55	70.8108
3	0	0	0	0	96.01	96.1114
4	0	0	0	0	94.56	96.1114
5	-1	1	1	-1	87.89	88.4721
6	1	-1	-1	1	84.17	84.2971
7	1	-1	1	1	78.37	79.6792
8	1	-1	-1	-1	90.84	93.4992
9	2	0	0	0	88.66	85.1621
10	-1	1	-1	-1	98.02	98.4125
11	0	0	0	2	86.21	84.0037
12	-1	1	-1	1	87.35	86.9754
13	0	0	0	0	95.11	96.1114
14	-2	0	0	0	72.02	73.1071
15	-1	-1	1	1	68.45	68.6404
16	0	0	-2	0	98.18	96.1587
17	0	0	2	0	81.99	81.6004
18	-1	-1	1	-1	79.24	78.7275
19	0	0	0	-2	98.71	98.5054
20	1	-1	1	-1	81.66	82.7438
21	-1	-1	-1	-1	88.38	87.0354
22	1	1	-1	-1	98.91	99.4288
23	-1	1	1	1	84.13	83.1725
24	0	0	0	0	95.86	96.1114
25	0	-2	0	0	75.36	73.6787
26	1	1	1	1	86.71	88.7638
27	1	1	1	-1	87.6	87.0408
28	0	0	0	0	97.86	96.1114
29	0	0	0	0	98.5	96.1114
30	1	1	-1	1	92.8	95.0142
31	0	0	0	0	94.88	96.1114

Table 3. ANOVA results for the developed second-order polynomial model

Source of variations	DF[a]	SS[b]	Adj-MS[c]	F-value	P-value	Critical F-value
Regression	14	2378.90	169.22	39.90	0.000	2.373
Linear terms	4	1479.37	369.842	86.85	0.000	
Square terms	4	751.30	187.824	44.11	0.000	
Interaction terms	6	148.24	24.706	5.80	0.002	
Residual error	16	68.13	4.258	-	-	-
Lack-of-Fit	10	54.37	5.437	2.37	0.151	4.060
Pure error	6	13.76	2.294	-	-	-
Total	30	2447.03	-	-	-	-

R^2= 97.22%, Adjusted R^2=94.78%

[a] Degree of freedom, [b] Sum of squares, [c] Adjusted mean square

2.4. Photodegradation experiments

In each experiment, the photodegradation abilities of the samples were evaluated by measuring the degradation of AR14 in aqueous solution under the visible irradiation. The visible light was irradiated from one 45 W visible Lamp (CCP, Iran). It must be mentioned that concentration of AR14, pH, amount of photocatalyst, and time were adjusted in each experiment to the values proposed by RSM according to Table 2. Typically, 50 mL solution of AR14 with appropriate concentration and photocatalyst was prepared and stirred at 300 rpm for 30 min in darkness to attain the adsorption equilibrium. Then, the homogeneous solution was irradiated under visible light. At the different time intervals proposed in Table 2, 2 mL of the solution was taken and filtered through a 0.45 μm membrane filter (Schleicher & Schuell, Germany). The concentration of the remaining AR14 was determined at λ_{max} 515 nm. The degradation efficiency (%) was calculated according to equation (2):

$$DE\ (\%) = \frac{C_0 - C}{C_0} \times 100 \qquad (2)$$

where C_0 is the initial concentration of AR14 and C is the concentration of AR14 after photoirradiation.

3. Results and discussion

3.1. Structural analysis

At first, the Co, Ni, Al, and Zn contents of the as-obtained materials were determined by using ICP measurements (Tables S1 and S2). The analytical results confirm that the Ni^{2+}/Co^{2+}, $(Ni^{2+} + Co^{2+})/Al^{3+}$, and Zn^{2+}/Al^{3+} molar ratios are comparative to that in the initial solution.

FTIR spectra of the pristine CNTs, acid-treated CNTs (CNT-COOH), Co-Ni-Al-LDH, Co-Ni-Al-LDH/ZnO/CNT nanohybrid, and ZnO/MMO/CNT nanohybrid are indicated in Figure 1. The FTIR spectrum of the CNT-COOH shows two absorption peaks located at 3433 cm^{-1}, 1700 cm^{-1}, and 1153 cm^{-1} corresponding to the vibration of OH, COOH, and C–O functional groups respectively, which do not appear in the spectrum of pristine CNT.[26] Therefore, the results show that the carboxylic and hydroxyl groups have been generated on the surface of the CNTs by nitric acid treatment. For Co-Ni-AlLDH/ZnO/CNT nanohybrid and ZnO/MMO/CNT nanohybrid, a broad band at 3456 cm^{-1} is attributed to the stretching vibration of OH groups in the brucite-like layers and the interlamellar water molecules. The broadening of the band is attributed to the hydrogen-bond formation. The peaks at 1364 cm^{-1} and 808 cm^{-1} are assigned to the v_3 stretching vibration and bending modes of the CO_3^{2-} groups in the samples. The band approximately at 428 cm^{-1} arising from O–M–O vibrations is observed. [28,29]

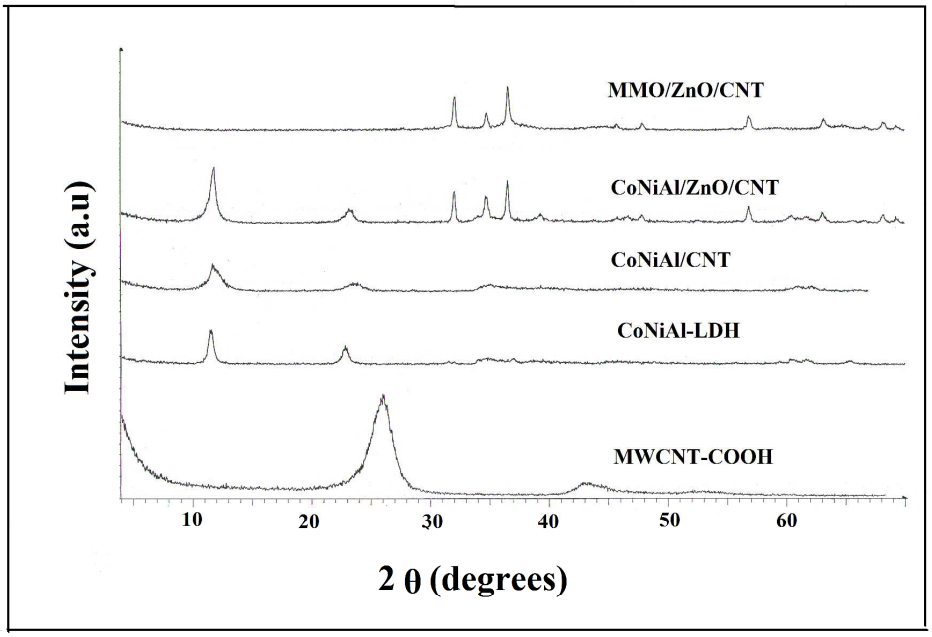

Figure 1. FT-IR spectrum of MWCNTs, MWCNT-COOH, Co-Ni-Al-LDH, Co-Ni-Al -LDH/ZnO/CNT, and ZnO/MMO/CNT nanohybrid.

The XRD patterns of MWCNT-COOH, Co-Ni-Al-LDH, Co-Ni-AlLDH/CNT, Co-Ni-Al-LDH/ZnO/CNT nanohybrid, and Co-Ni-Al-Zn/CNT mixed metal oxide (ZnO/MMO/CNT) nanohybrid are shown in Figure 2. The XRD patterns of Co-Ni-Al-LDH, Co-Ni-Al-LDH/CNT, and Co-Ni-AlLDH/ZnO/CNT exhibit the characteristic reflections of the LDH structure. The peaks at 11.44°, 22.77°, 34.16°, 60.3°, and 61.5° are indexed as planes (003), (006), (110), and (113). In the XRD patterns of Co-Ni-Al-LDH, Co-Ni-Al-LDH/ZnO/CNT, these reflections are indexed to a typical hydrotalcite-like structure (JSPDC No. 15-0087).[30] In case of Co-Ni-Al-LDH/ZnO/CNT, reflection peaks in the range of $2\theta = 32^{\circ} - 36^{\circ}$ (Figure 2 c and d) are attributed to the zinc hydroxide and ZnO phase (JCPDS card no. 36-1451). The disappearance of (002) and (101) diffraction peaks of the CNT-COOH (graphite layers) in the Co-Ni-AlLDH/CNT, Co-Ni-

Al-LDH/ZnO/CNT, and ZnO/MMO/CNT nanohybrids confirm the formation of nanohybrides and it can be indicated that the MWCNT-COOH incorporates into the LDHs and ZnO/MMO

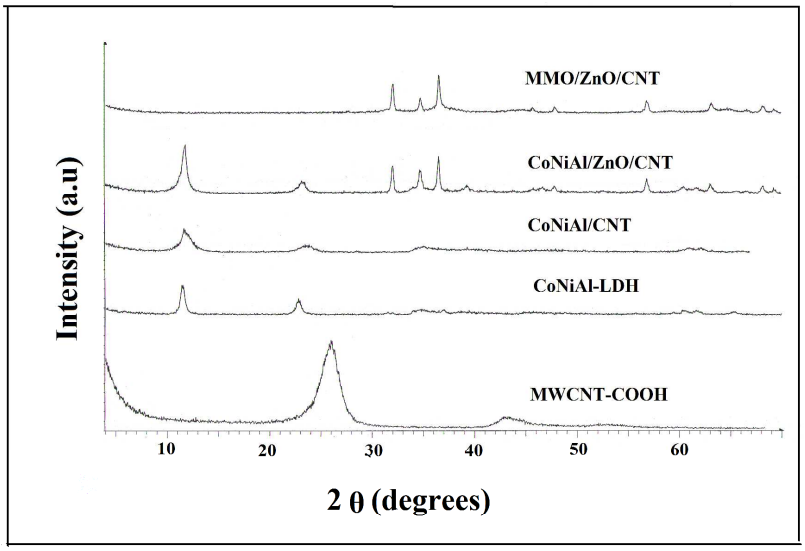

Figure 2. XRD patterns of MWCNT-COOH, Co-Ni-Al-LDH, Co-Ni-Al-LDH/CNTs, Co-Ni-Al-LDH/ZnO/CNT, and ZnO/MMO/CNT nanohybrid.

networks. According to the results , the unit cell parameters and interlayer distances are very similar to the original LDH, confirming that the zinc hydroxide is adsorbed by the surface of the LDHs rather than intercalated between the interlayers. After the calcination of the Co-Ni-Al-LDH/ZnO/CNT nanohybrid at 300 °C, the layered structure of Co-Ni-Al-LDH is completely destroyed and ZnO/MMO/MWCNT nanohybrid is formed. In the case of ZnO/MMO/MWCNT nanohybrid most of the diffraction peaks may be indexed to the Wurtzite of ZnO (JCPDS card no. 36-1451). Because of low calcinations temperature (300 °C) of Co-Ni-Al-LDH/ZnO/CNT and consequently low crystallinity of metal oxides, as shown in XRD pattern , no peak assigned

to the cobalt oxide, nickel oxide, and aluminum oxide were observed in the ZnO/MMO/MWCNT nanohybrid. These results are similar to those reported by Klemkaite et al. [31]

Based on our results, the photocatalytic activity of ZnO/MMO/MWCNT sharply depends on the calcinations temperature of Co-Ni-Al-LDH/ZnO/CNT. The best photocatalytic activity of ZnO/MMO/MWCNT nanohybrid is achieved in calcination temperature of 300 °C. Increasing of calcination temperature of Co-Ni-Al-LDH/ZnO/CNT to higher than 300 °C results in decrease in photocatalytic activity of derived ZnO/MMO/MWCNT nanohybrid. This fact may be related to the increasing of grain size of metal oxides in the ZnO/MMO/MWCNT nanohybrid by increasing the calcinations temperature.

Figure 3 (a and b) shows SEM images of Co-Ni-Al-LDH and ZnO/MMO/CNT nanohybrid. Figure 3a confirms the formation of crystals with perfect sheet shapes and LDH sheets, in which the predominantly smooth textures have been produced.

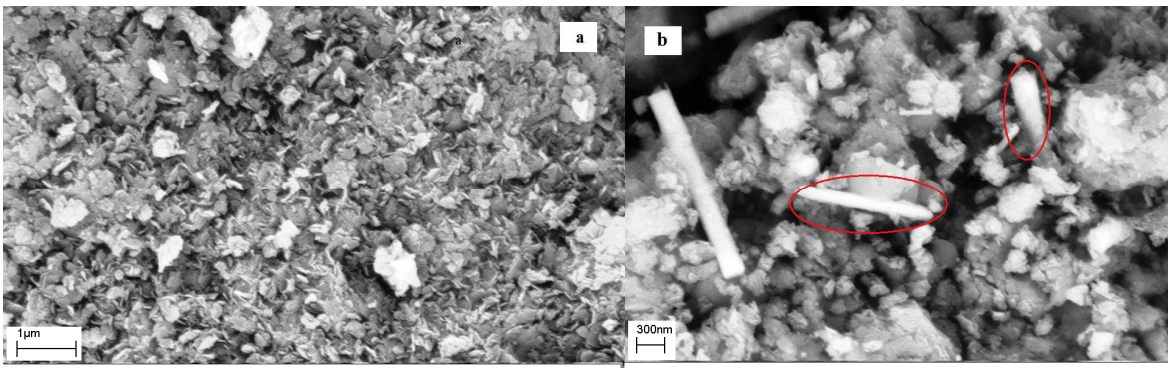

Figure 3. SEM micrographs of NiCoAl-LDH and ZnO/MMO/CNT nanohybrid.

In the SEM image of the ZnO/MMO/CNT nanohybrid (Figure 3b), ZnO nanorods can be easily distinguished (red circles). It is well known that the final morphology of ZnO crystals is related to both their intrinsic crystal structure and external factors. The catalytic activity of the ZnO nanostructures possesses a sequence of nanorods > nanoflowers > nanopyramids > nanoprisms.[32] Figure 4 shows the TGA and DTG curves of NiCoAl-LDH/CNT and ZnO/ NiCoAl-LDH /CNT nanohybrid samples. Both samples have similar thermal decomposition behavior. For NiCoAl-LDH/CNT, three degradation stages are distinguishable in TGA. Below 180 °C, water releases from the surface and LDH interlayer. The temperature range of 180–270 °C corresponds to the second stage with the dehydration of the brucite-like layers, and the final stage is the decomposition of carbonate ions in the interlayer occurring in the range of 270–500 °C. The DTG curve shows two distinct peaks for both samples. The first peak around 110 °C is ascribed to the removal of water. The peak at 270 °C for both of the samples corresponds to the decomposition of carbonate ions in the interlayer of LDH. The small peak in the DTG curve of ZnO/ NiCoAl-LDH /CNT nanohybrid sample arises from the dehydration of LDH layers. For the NiCoAl-LDH sample, the small peak was absent in the DTG curve, remarking the presence of an overlap between the dehydration and decomposition of carbonate ions in these samples.[28]

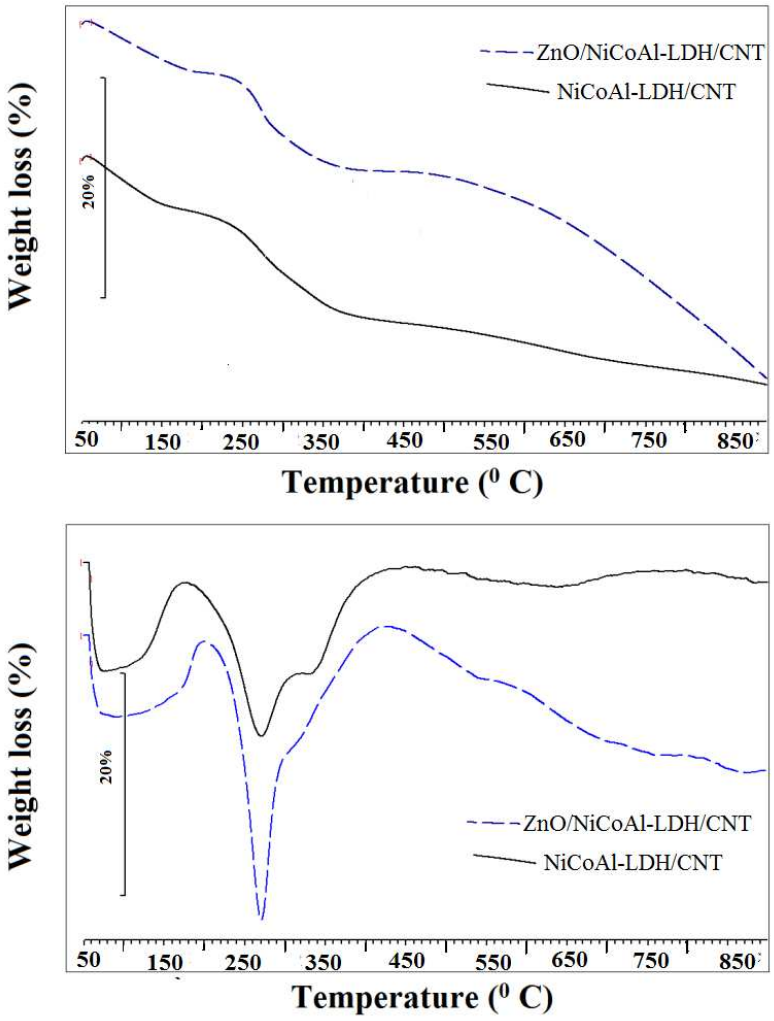

Figure 4. (a) TGA and (b) DTG curves of NiCoAl-LDH/CNT and ZnO/ NiCoAl-LDH /CNT nanohybrid.

3.2. Photocatalytic performance of ZnO/MMO/CNT nanohybrid under visible light irradiation

The photochatalytic activity of prepared ZnO/MMO/CNT nanohybrid was compared with ZnO, TiO_2- P25, and NiCoAl-LDH/ZnO/CNT nanohybrid at a fixed AR14 concentration (50 mg L^{-1}**)** and at the same photocatalyst content. Based on the experimental results presented in Figure 5, the highest degradation efficiency was achieved using mixed metal oxide (ZnO/MMO)

nanohybrid catalyst under the visible light. The results also demonstrated that the ranking of removal efficiency was in the order of ZnO/MMO/CNT nanohybrid- vis > TiO_2- vis > CoNiAl/ZnO/CNT nanohybrid- vis > ZnO- vis > ZnO/MMO/CNT nanohybrid in dark > visible light only.

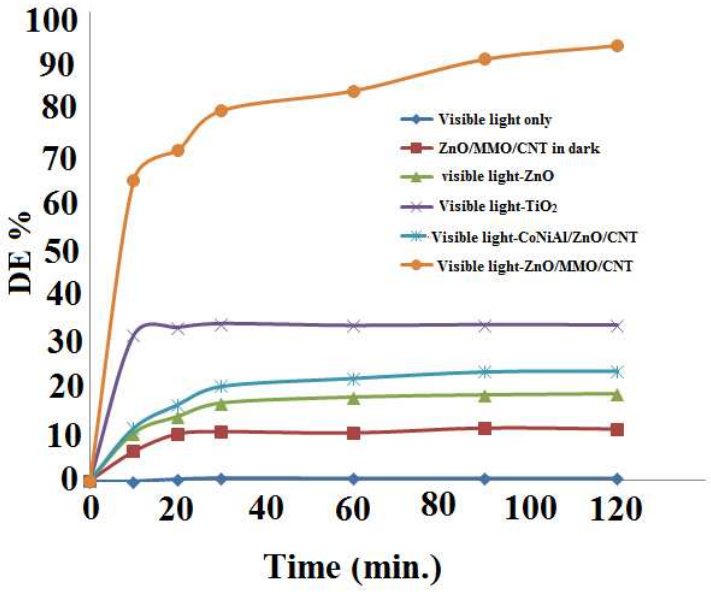

Figure 5. Comparison of photocatalytic activity of ZnO/MMO/CNT, CoNiAl/ZnO/CNT, with ZnO, TiO_2- P25, and NiCoAl-LDH/MWCNT nanohybrid in the removal of Acid Red 14 initial pH = 5.5, [AR14] = 50 mg $^{-1}$ and catalyst dosage = 0.01gr.

The photodegradation of AR14 was negligible in the direct photolysis (visible light only). The removal of dye was less than 10% in the absence of ZnO/MMO/CNT nanohybrid which indicates that light decomposition of AR14 in ZnO/MMO/CNT-visible light process is attributed to photocatalytic properties of ZnO/MMO/CNT nanohybrid. The photocatalytic activity of

ZnO/MMO/CNT nanohybrid was also compared with ZnO and TiO_2- P25 as typical reference photocatalysts. As seen in Figure 5, the removal efficiency of ZnO/MMO/CNT nanohybrid (96.2%) is considerably greater than that of ZnO (18.57%) and TiO2- P25 (28.14%). These findings may be attributed to the fact that the coupling of semiconductors provides different band-gaps and energy levels which is an interesting way to increase the charge separation and expand the energy range of photoexcitation for photocatalytic process. To verify the obtained results, the UV/vis diffuse reflectance spectra (DRS) technique was used. The DRS spectra of NiCoAl-ZnO-LDH/CNT, ZnO/MMO/CNT nanohybrid, and ZnO nanoparticle are illustrated in Figure 6. Both samples show one absorption edge around 350 nm that is related to the absorption edges of ZnO, but ZnO/MMO/CNT nanohybrid shows another peak emerged at 400–800 nm which represents the ability of the visible response. The phenomena imply good ability of ZnO/MMO/CNT nanohybrid for utilizing sunlight owing to its wide light-adsorption range. Also, the optical band gap energies (E_g) of the prepared NiCoAl-Zn-LDH/CNT, ZnO/MMO/CNT nanohybrid, and ZnO were determined by UV-vis DRS, and the obtained DRS results are reported according to the Kubelka–Munk function (3).[33, 34]

$$\alpha = \frac{(1-R)^2}{2R} \qquad (3)$$

where R is the reflectance and α is the Kubelka–Munk function.

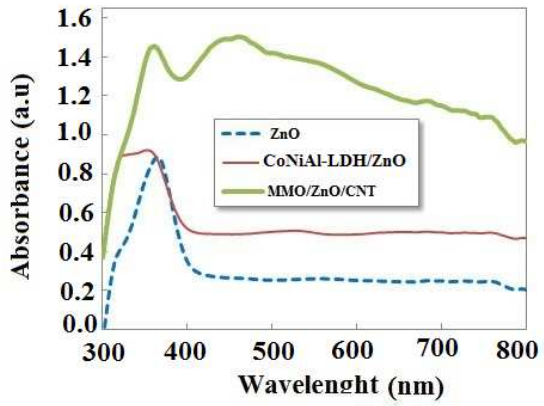

Figure 6. UV–vis diffuse reflectance spectra of ZnO/MMO/CNT, Co-Ni-Al-LDH/ZnO/CNT, and ZnO

As shown in Figure 7, the optical bandgap energies of the prepared NiCoAl-Zn-LDH/CNT, ZnO/MMO/CNT nanohybrid, and ZnO can be derived from UV-vis DRS data by plotting $(\alpha h\nu)^2$ against photon energy ($h\nu$), followed by extrapolation of the linear part of the spectra to the energy ($h\nu$) axis. The calculated values of the bandgap energies for NiCoAl-Zn-LDH/CNT and ZnO were 3.17 and 3.21 eV respectively, but for ZnO/MMO/CNT nanohybrid, two band gap energies in 2.15 and 2.75 eV were obtained which confirms a red shift in the absorbance spectra of ZnO/MMO/CNT nanohybrid.

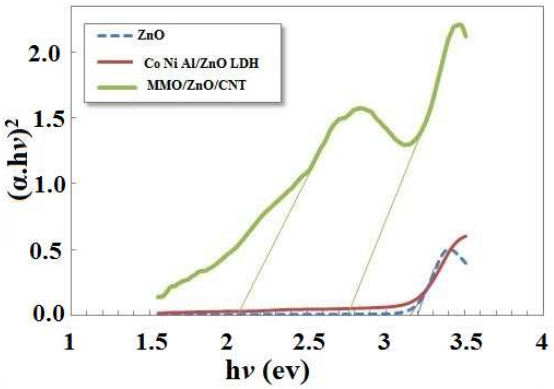

Figure 7. Kubelka–Munk transformed reflectance spectra for ZnO/MMO/CNT, Co-Ni-Al-Zn/CNT, and ZnO

Based on some literature data [35-38], during a photocatalytic process equipped with mixed metal oxides irradiated with ultra violet or visible light, degradation of an organic molecule is generally operated by the formation of the electron/hole pairs on the surface of the photocatalyst. ZnO/MMO/CNT has high adsorbing capacity as well as high efficiency for the photocatalytic degradation. The pre-adsorption of the substrate (dye) onto the photocatalyst and the photoexcitation of the semiconductor followed by the formation of the electron/hole pairs are two prerequisites for highly efficient degradation [24]. The photogenerated valence band holes react with either water (H_2O) or hydroxyl ions (OH^-) adsorbed on the catalyst surface. Then, highly reactive hydroxyl radicals ($OH^\bullet$) are produced, that promotes the degradation of target pollutants. According to some references [39], in the case of acid red 14, the bonds of N=N and C-N are the major targets for hydroxyl radicals (•OH) and photon electrons (e−) during the degradation of azo dye compounds. Besides, dissolved oxygen can capture photogenerated electrons from the conduction band to generate superoxide ions ($^\bullet O_2^-$). Based on recently reported researches [40], $^\bullet O_2^-$ has been proposed as the major photocatalytic oxidant in the photocatalytic oxidation of azo dyes under light irradiation. The superoxide ions can then react with water to produce hydrogen peroxide and hydroxyl ions. Cleavage of hydrogen peroxide by the conduction band electrons yields further hydroxyl radicals and hydroxyl ions. The hydroxyl ions can react with the valance band holes to from additional hydroxyl radicals. The tentative photodegradation mechanism of acid red 14 by MMO/ZnO/CNT nanohybrid under visible light irradiation is given by equations (4)-(9).

$$\text{MMO/ZnO/CNT nanohybrid} + h\upsilon \rightarrow (e^-_{CB} + h^+_{VB})\ \text{MMO/ZnO/CNT nanohybrid} \quad (4)$$

$$h^+ + H_2O \rightarrow H^+ + {}^\bullet OH \quad (5)$$

$$h^+ + OH^- \rightarrow {}^\bullet OH \quad (6)$$

$$e^- + O_2 \rightarrow {}^\bullet O_2^- \quad (7)$$

$$^\bullet O^-_2 + H_2O + H^+ \rightarrow H_2O_2 + OH^- \quad (8)$$

$H_2O_2 + e^- \rightarrow {}^{\bullet}OH + OH^-$ (9)

The resulting ˙OH radical, being a very strong oxidizing agent (standard redox potential + 2.8 V), and the degradation of dye can be achieved by their reaction with hydroxyl radicals (•OH) or by direct attack from the valence band holes. Scheme 1 shows the schematic diagram of a visible light photocatalytic tentative mechanism with ZnO/MMO/CNT nanohybrid.

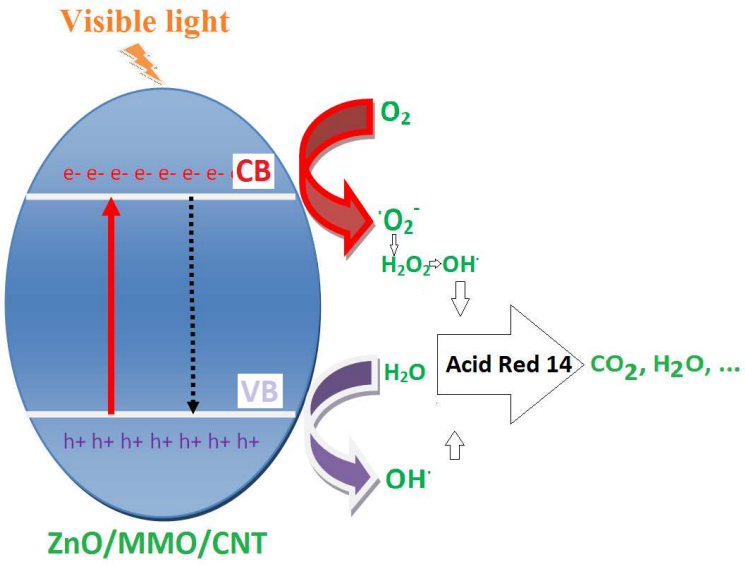

Scheme 1. Schematic representation of visible light photocatalytic process in the presence of ZnO/MMO/CNT nanohybrid.

3.3. RSM model development and its significant analysis

Based on the obtained results from CCD, the second-order regression (Eq.(10)) with the coded variable was achieved by ordinary least square estimation.[41]

$$y = 96.1114 + 3.0137x_1 + 5.1154 - 3.6396x_3 - 3.6254x_4 - 4.2442x_1^2 - 3.0505x_2^2 - 1.8080x_3^2 - 1.2142x_4^2 - 1.3619x_1x_2 - 0.6919x_1x_3 + 1.7556x_1x_4 - 0.4081x_2x_3 + 1.1969x_2x_4 + 1.5344x_3x_4$$ (11)

The predicted degradation efficiency obtained from Eq. (10) is provided in Table 2. The significance and adequacy of the model was tested using the analysis of variance (ANOVA) calculation and the obtained results are summarized in Table 3. According to ANOVA analysis, the Fisher's F-value of regression (equal to 39.9) was considerably much higher than the critical F-value confirming the significant of the obtained second-order polynomial model. [41] It was also revealed from ANOVA results that all model terms, including first and second order main effects and interaction effects, are significant because of small p-values (significant probability values). In statistics, higher F-value or lower p-value (<0.05) for one term is considered to be significant. Moreover, P-value greater than 0.05 for the lack of a fit test (LOF) demonstrates insignificant LOF for the obtained model. The comparison of experimental and predicted degradation efficiencies (R^2= 97.22%, adj-R^2=94.78%) reveals that the model suitably describes the relation between the response and the variables.[42] In addition to three mentioned criteria for evaluating the model adequacy, the residuals were utilized to survey the model significance. As shown in Figure 8, a random pattern of residuals in Figure 8a and straight line of residuals in Figure 8b indicate the normal and independent distribution of residuals. It means that the model is a good predictor.

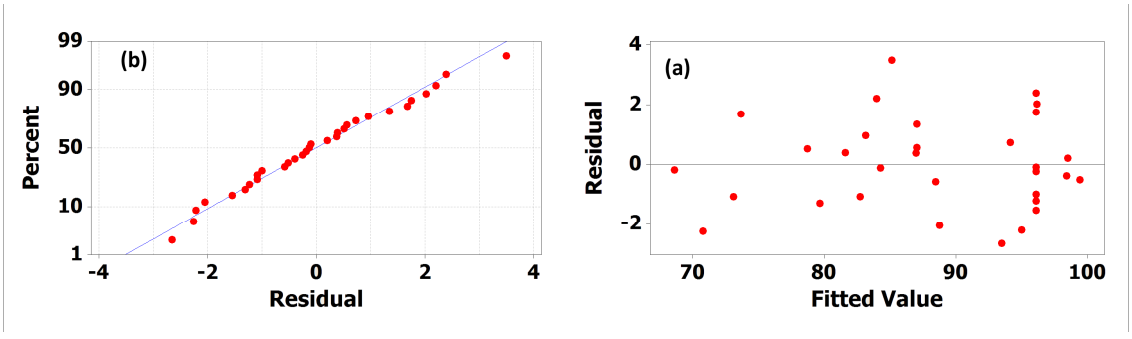

Figure 8. Residual plots for removal efficiency of AR14 (a) normal probability plots of residuals and (b) residuals versus fits plots

The student's t distribution and Pareto analysis were utilized to evaluate the significance of the model terms (Table 4). The P-values were considered as the checking tools for significant term

Table 4. Model coefficients corresponding P-values and Pareto analysis results

Coefficient		Coefficient estimate	T-value	P-value	Percentage effects of model terms, %
b0	Constant	96.1114	123.228	0.000	-
b1	x_1	3.0137	7.155	0.000	8.82
b2	x_2	5.1154	12.144	0.000	25.41
b3	x_3	-3.6396	-8.641	0.000	12.86
b4	x_4	-3.6254	-8.607	0.000	12.76
b11	x_1 x_1	-4.2442	-10.999	0.000	17.49
b22	x_2 x_2	-3.0505	-7.905	0.000	9.04
b33	x_3 x_3	-1.8080	-4.685	0.000	3.17
b44	x_4 x_4	-1.2142	-3.147	0.006	1.43
b12	x_1 x_2	-1.3619	-2.640	0.018	1.80
b13	x_1 x_3	-0.6119	-1.186	0.253	0.36
b14	x_1 x_4	1.7556	3.403	0.004	2.99
b23	x_2 x_3	-0.4081	-0.791	0.440	0.16
b24	x_2 x_4	1.1969	2.320	0.034	1.39
b34	x_3 x_4	1.5344	2.974	0.009	2.29

determination. P-values smaller than 0.05 indicate that the coefficients of this model are significant. In addition to student's t distribution, the percentage effect of each term was determined with the Pareto analysis, which calculates the percentage effect of each term on the response. [27,43] Based on the results presented in Table 4, all linear and square terms of the model are important, but the importance of irradiation time (25.41%) and ZnO/MMO/CNT× ZnO/MMO/CNT (17.49 %) have the main effect on the degradation of AR14. The interaction

terms are not of much importance due to higher p-values. Among the interaction terms, x1x4 and x3x4 interactions are relatively significant.

The 3-dimensional response surface and 2-dimensional counter plots (Figure 9) were utilized to survey the interaction and individual effects of catalyst dosage, pH, and contact time on removal efficiency. Figure 9 illustrates the effect of the catalyst dosage and irradiation time on the degradation efficiency of AR14. The enhancement of AR14 degradation is observed with increasing the MMO/ZnO/CNT nanohybride dosage. It can be concluded that the total active surface area increases with increasing catalyst dosage. As seen in Figure 9, at the higher loading of optimum concentration of the catalyst, the degradation efficiency of AR14 is decreased. This observation can be explained on the basis of the total active sites on the catalyst surface and the penetration of light into suspension. Due to an increase in the turbidity of the suspension, decrease in light penetration occurs and hence, the photoactivated volume of suspension decreases.

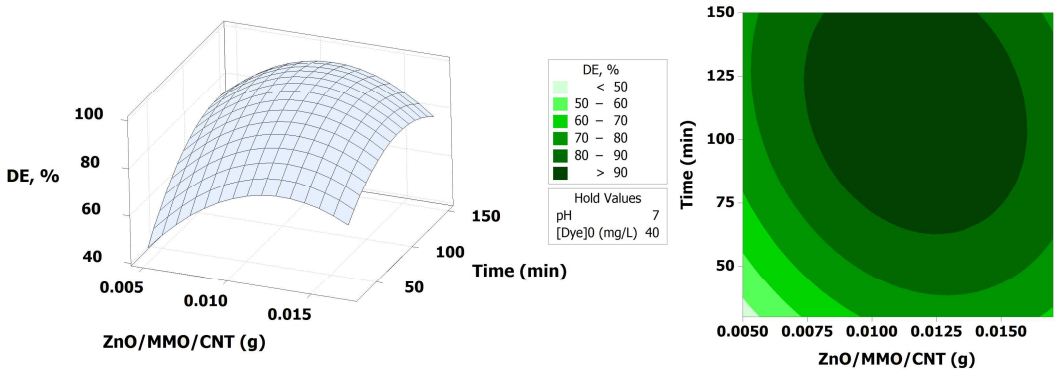

Figure 9. Contour and surface plots showing the effect of the catalyst dosage and irradiation time on the degradation efficiency of AR14 by ZnO/MMO/CNT nanohybrid (T = 26 °C, pH= 7).

Figure 10 shows the effects of initial concentration of dye and irradiation time on the degradation efficiency of AR14. The degradation efficiency of AR14 decreased with the increase of initial concentration of dye. When initial concentration increases, more organic substances are adsorbed on the surface of the catalyst. Therefore, there are only a few active sites for the photodegradation process. Furthermore, when the concentration of dye solution increases, the photons get intercepted before they can reach the catalyst surface.

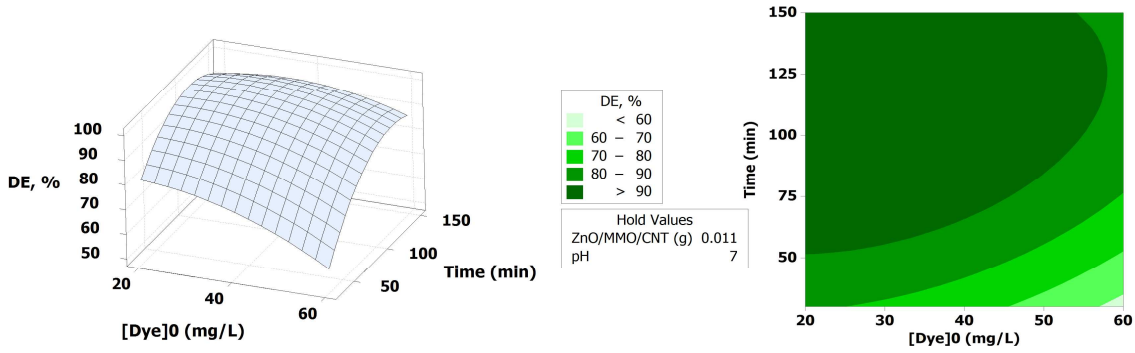

Figure 10. Contour and surface plots showing the effects of initial concentration of dye and irradiation time on the degradation efficiency of AR14 by ZnO/MMO/CNT nanohybrid ($[Dye]_0$= 40 mg/L, catalyst dosage = 0.011 gr).

Figure 11 reveals the effects of initial pH and contact time on the degradation efficiency of AR14. In general, pH plays an important role in the determination of the surface charge properties of the photocatalyst and the charge of the dye molecules, which is effective in the total active surface sites available for both the reactant and the photon absorptions. On the other hand, the zero charge point of the catalyst is important in the photocatalytic processes. Theoretically, at pH <point of zero charge(PZC), the surface gets positively charged, which enhances the adsorption of negatively charged dye anions through electrostatic forces of the attraction. At pH> (PZC), the surface of the catalyst gets negatively charged, which favors the adsorption of cationic dye. In this study, the PZC of MMO/ZnO/CNT nanohybrid was

determined 5.50. In Figure 10, it can be observed that the degradation efficiency of AR14 increases with decrease in initial pH value. At low pH values, the H^+ ions with the excess concentration tend to easily interact with the azo group (–N=N–) containing lone-pair electrons. On the other hand, in low pH value electrostatic attraction is formed between negatively charged AR14 and positively charged MMO/ZnO/CNT nanohybrids. Also, decrease is observed in the degradation efficiency at initial pH that is higher than the PZC. There may be a strong Columbic repulsion between the negatively charged surface of MMO/ZnO/CNT nanohybrids and the negatively charged AR14 dye molecules.

According to the obtained polynomial model, optimum values of the photocatalyst dosage, pH, and irradiation time were 0.009 g, 4.12, and 150 min respectively. The predicted degradation efficiency value of AR14 at optimum conditions was ≈99.41% and the corresponding experimental value obtained was 98.08%.

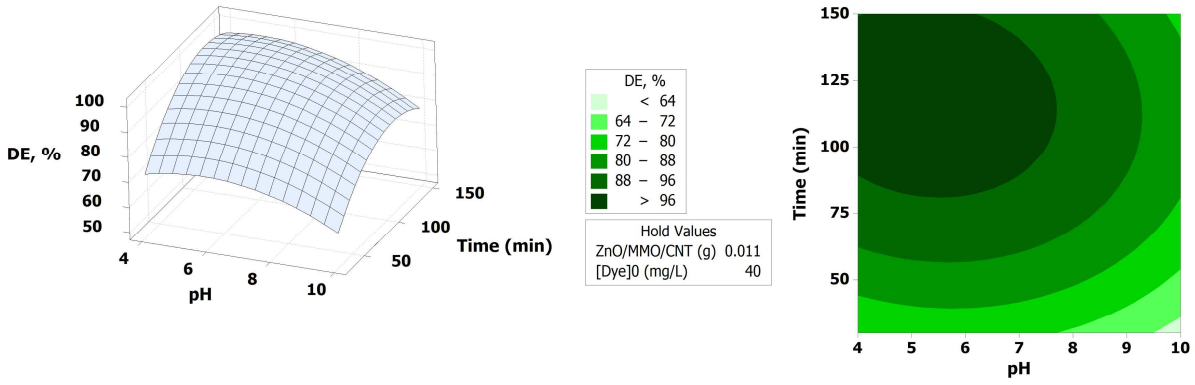

Figure 11. Contour and surface plots showing the effects of initial pH and contact time on the efficiency of AR14 by ZnO/MMO/CNT nanohybrid ($[Dye]_0$= 40 mg/L, catalyst dosage = 0.011 gr).

3.4. Photocatalyst recycling and photostability

Consecutive application of the photocatalyst and maintenance of its photocatalytic activity is an important factor in long-term use of the photocatalyst in full-scale applications. To this end, the reusability of MMO/ZnO/CNT nanohybrid was tested with AR14 concentration of 20 mg/L, photocatalyst dosage of 0.009 g/L, and reaction time of 150 min. Five consecutive experimental runs were carried out to define the loss in the degradation efficiency of AR 14 after each step. As shown in Figure 12, the degradation efficiency decreased from 96% to 84.55% after the fifth run. Therefore, negligible decrease in the degradation efficiency after five recycled experiments indicates that the MMO/ZnO/CNT nanohybrid can be an efficient photocatalyst for the degradation of organic dyes with high reusability potential.

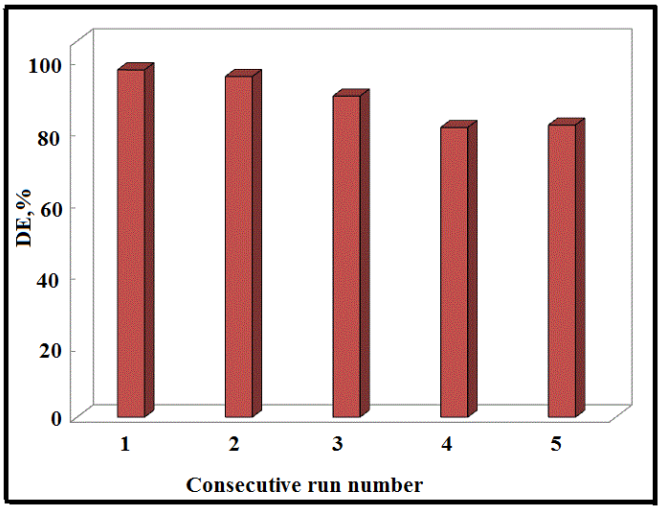

Figure 12. Reusability of MMO/ZnO/CNT nanohybrid within five consecutive experimental runs. AR14 concentration of 20 mg/L, photocatalyst dosage of 0.009 g/L, and reaction time of 150 min.

It has been reported that pure ZnO semiconductor suffers from the photoinduced dissolution (photocorrision) when ZnO is irradiated by the UV light.[45,45] Based on our previously reported

results, ZnO/MMO exhibits better photostability under UV irradiation than pure ZnO [28]. In addition, doped or decorated ZnO shows almost no photoactivity loss under visible light.[46] In fact, based on the degradation efficiency of ZnO/MMO/CNT nanohybrid photocatalyst under visible light, we can conclude that the ZnO/MMO/CNT assembles prevent ZnO semiconductor from photocorrosion during the photocatalytic process.

3.5. Mineralization and MMO/ZnO/CNT nanohybrid performance under sunlight

Apart from degradation process, mineralization of AR14 and its photocatalytic degradation to carbon dioxide, water, and mineral ions were studied by measuring TOC value of the solution as the function of the reaction time. Therefore, the degradation efficiency for color is compared with TOC that is obtained in the photocatalytic process, which consists of MMO/ZnO/CNT nanohybrid as the catalyst under optimized operational parameters (initial AR14 concentration = 20 mg/L, contact time = 120 min, concentration of catalyst = 0.009 g/L, and initial pH = 4.12). The results show that after reaction for 120 min, degradation and TOC removal efficiencies were 98.50% and 63% respectively. The results indicate that, although dye mineralization is lower than degradation, a significant TOC removal can be achieved by prolonging the treatment time to a few hours.

To verify good ability of ZnO/MMO/CNT nanohybrid for utilizing the sunlight, an experiment was carried out under sunlight at optimized operational parameters (initial AR14 concentration = 20 mg/L, irradiation time = 210 min, ZnO/MMO/CNT nanohybrid content= 0.009 g/L, and initial pH=4.12). The results indicate that after 210 min process under sunlight, more than 75.25% of dye was removed. Although removal efficiencies under sunlight is lower than visible light, this result is acceptable and indicates that the absorption edge of ZnO/NiCoAl-

LDH/CNT nanohybrid shifts to the visible region in mixed metal oxide (ZnO/MMO/CNT) nanohybrid which may be beneficial in increasing capability of photocatalytic activity in sunlight.

4. Conclusion

The present study provides a facile and effective approach for assembling mixed metal oxide ZnO/MMO/CNT nanohybrid with excellent photodegradation performance under visible light. The photocatalytic activity under the visible light irradiation of ZnO/MMO/CNT nanohybrid was much higher than that of ZnO and TiO_2- P25 as typical reference photocatalysts. Moreover, the photodegradation of AR14 by ZnO/MMO/CNT nanohybrid was modeled and optimized using RSM. The optimum conditions proposed by the RSM for the maximum removal of AR14 were adsorbent dosage of 0.011 g, initial pH equal to 4.12, and contact time of 120 min. The results show that the ZnO/MMO/CNT nanohybrid has good ability to be utilized as a photocatalyst in sunlight because of its narrow band gap energy. Then the reusability study was performed, and its results demonstrated the capability of the ZnO/MMO/CNT nanohybrid to be used in several experimental cycles. Finally, this work may provide useful information in the development of some effective mixed metal oxide catalysts from LDH for the degradation of pollutants under visible-light.

Acknowledgment

The authors are grateful to the Azarbijan Shahid Madani University for financial supports.

Notes and references

1 H. Choi, S. R. Al-Abed, D.D. Dionysiou, E. Stathatos and P. Lianos, Chapter 8 TiO_2-BasedAdvanced Oxidation Nanotechnologies for Water Purification and Reuse, in: C.E. Isabel, I.S. Andrea (Eds.) Sustainability Science and Engineering, Elsevier, 2010, pp. 229-254.

2 M.A. Fox and M.T. Dulay, *Chem. Rev.*, 1993, **93,** 341-357.

3 M.R. Hoffmann, S.T. Martin, W. Choi, D.W, *Chem. Rev.,* 1995, **95** , 69-96.

4 A.R. Khataee and M.B. Kasiri, *J. Mol. Catal. A: Chem.*, 2010, **331**, 86-100.

5 O. Carp, C.L. Huisman and A. Reller, *Prog. Solid State Chem.,* 2004, **32**, 33-177.

6 A. Di Paola, E. García-López, G. Marcì and L. Palmisano, *J. Hazard. Mater.,* 2012, **211–212,** 3-29.

7 H. Lachheb, E. Puzenat, A. Houas, M. Ksibi, E. Elaloui, C. Guillard and J.-M. Herrmann, *Appl. Catal., B,* 2002, **39**, 75-90.

8 X. Chen and S. S. Mao, *Chem. Rev.,* 2007, **107** 2891-2959.

9 W. Sun, S. Zhang, Z. Liu, C. Wang and Z. Mao, *Int. J. Hydrogen Energy.,* 2008, **33**, 1112-1117.

10 L. Zhang, X. Li, Z. Chang and D. Li, *Mater. Sci. Semicond. Process.,* 2011, **14**, 52-57.

11 Y.-K. Lai, J.-Y. Huang, H.-F. Zhang, V.-P. Subramaniam, Y.-X. Tang, D.-G. Gong, L. Sundar, L. Sun, Z. Chen and C.-J. Lin, *J. Hazard. Mater.,* 2010, **184**, 855-863.

12 M. Zhou, J. Yu, S. Liu, P. Zhai and L. Jiang, *J. Hazard. Mater.,* 2008, **154,** 1141-1148.

13 P. Wongkalasin, S. Chavadej and T. Sreethawong, *Colloids Surf., A.,* 2011, **384**, 519-528.

14 X. Li, H. Zhao, X. Quan, S. Chen, Y. Zhang and H. Yu, *J. Hazard. Mater.,* 2011, **186**, 407-415.

15 V. Iliev, D. Tomova, L. Bilyarska, G. Tyuliev, *J. Mol. Catal. A: Chem.,* 2007, **263**, 32-38.

16 V. Keller and P. Bernhardt, F. Garin, *J. Catal.,* 2003, **215**, 129-138.

17 C. Hu, Y. Lan, J. Qu, X. Hu and A. Wang, *J. Phys. Chem. B*, 2006, **110**, 4066-4072.

18 F. Wang and K. Zhang, *J. Mol. Catal. A: Chem.,* 2011, **345**, 101-107.

19 D. Eder and A. H. Windle, *Adv. Mater.,* 2008, **20**, 1787-1793.

20 X. Ma, M. Tsige, S. Uddin, S. Talapatra, Mater. Express., 2011, **1**, 183-200.

21 S. Bai, H. Li, Y. Guan and S. Jiang, *Appl. Surf. Sci.,* 2011, **257**, 6406-6409.

22 H. Choi, E. Stathatos and D. D. Dionysiou, *Desalination*, 2007, **202**, 199-206.

23 J. Wang, J. Li, Y. Xie, C. Li, G. Han, L. Zhang, R. Xu and X. Zhang, *J. Environ. Manage.*, 2010, **91,** 677-684.

24 Z. Rezvani, M. Sarkarat, A.R. Khataee and K. Nejati, *Cryst. Res. Technol.,* 2012, **47**, 1172-1184.

25 S. Mustafa, B. Dilara, K. Nargis, A. Naeem and P. Shahida, *Colloids Surf. A.,* 2002, **205**, 273-282.

26 C.G. Salzmann, S.A. Llewellyn, G. Tobias, M. A. H. Ward, Y. Huh and M. L. H. Green, Material, *Adv. Mater.,* 2007, **19,** 883-887.

27 A. R. Amani-Ghadim, S. Aber, A. Olad and H. Ashassi-Sorkhabi, *Chem. Eng. Process.,* 2013, **64,** 68-78.

28 A. A. A. Ahmed, Z. A. Talib, M. Z. bin Hussein and A. Zakaria, *J. Solid State Chem.,* 2012, **191**, 271-278.

29 M. Lakraimi, A. Legrouri, A. Barroug, A. De Roy and J. P. Besse, *Mater. Res. Bull.,* 2006, **41**, 1763- 1774.

30 J. Xu, S. Gai, F. He, N. Niu, P. Gao, Y. Chen and P. Yang, *Dalton Trans.*, 2014, **43**, 11667-

11675.

31 K. Klemkaite, I. Prosycevas, R. Taraskevicius, A. Khinsky and A. Kareiva1, *Cent. Eur. J. Chem.,* 2011, **9**, 275-282.

32 F. Ahmed, N. Arshi, M. S. Anwar, R. Danish and B. H. Koo, *RSC Adv.,* 2014, **4**, 29249-29263

33 H. M. Ali, M. M. Abou-Mesalam and M. M. El-Shorbagy, *J. Phys. Chem. Solids.,* 2010, **71**, 51-55.

34 K. H. Reddy, S. Martha and K.M. Parida, *Inorg. Chem.,* 2013, **52,** 6390-6401.

35 J. M. Herrmann, Top. Catal., 2005, **34**, 49-65.

36 J. Chang and E. R. Waclawik, *Cryst. Eng. Comm*., 2012, **14**, 4041-4048.

37 M. S. Mashkour, A. F. Alkaim, L. M. Ahmed and B. H. Koo, RSC Advances, 2014, **4**, 29249-29263

38 F. H. Hussein, Int. J. Chem. Sci., 2011, **9**, 969-977.

39 S. Xia, X. Zhou, W. Shi, G. Pan and Z. Ni, *J. Mol. Catalysis A: Chemical*, 2014,**392**, 270–277

40 X. An, H. Liu, J. Qu, S. J. A. Moniz and J. Tang, *New J. Chem.,* 2015,**39**, 314-320.

41 A. R. Khataee, M. Zarei and S.K. Asl, *J. Electroanal. Chem.,* 2010, **648,** 143-150.

42 M.S. Bhatti, A.S. Reddy and A.K. Thukral, *J. Hazard. Mater.,* 2009, **172**, 839-846.

43 M. Zarei, A. Niaei, D. Salari and A. Khataee, *J. Hazard. Mater.,* 2010, **173**, 544-551.

Table of contents entry

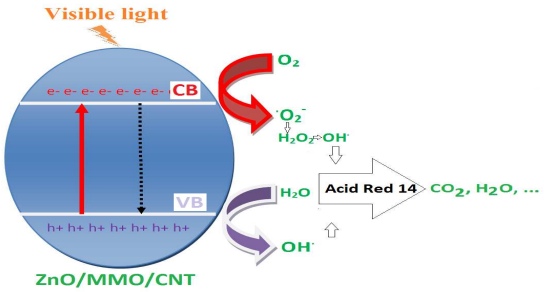

A facile and effective approach for assembling ZnO/MMO/CNT nanohybrid with excellent photodegradation performance under visible light is reported.